

## PAPER

Cite this: *Nanoscale Adv.*, 2024, 6, 3199

# Efficient cationic dye removal from water through *Arachis hypogaea* skin-derived carbon nanospheres: a rapid and sustainable approach†

Aman Sharma,<sup>a,c</sup> Jyothi Mannekote Shivanna,<sup>b</sup> Abdullah N. Alodhayb<sup>d</sup> and Gurumurthy Hegde<sup>a,c\*</sup>

The present study investigates the potential of *Arachis hypogaea* skin-derived carbon nanospheres (CNSs) as an efficient adsorbent for the rapid removal of cationic dyes from aqueous solutions. The CNSs were synthesized through a facile, cost-effective, catalyst-free and environmentally friendly process, utilizing *Arachis hypogaea* skin waste as a precursor. This is the first reported study on the synthesis of mesoporous carbon nanospheres from *Arachis hypogaea* skin. The structural and morphological characteristics of the CNSs were confirmed by different nano-characterization techniques. The adsorption performance of the carbon nanospheres was evaluated through batch adsorption experiments using two cationic dyes—methylene blue (MB) and malachite green (MG). The effects of the initial dye concentration, contact time, adsorbent dosage, and pH were investigated to determine the optimal conditions for dye removal. The results revealed that the obtained CNSs exhibited remarkable adsorption capacity and rapid adsorption kinetics. Up to ~98% removal efficiency was noted for both dyes in as little as 2 min for a 5 mg L<sup>-1</sup> dye concentration, and the CNSs maintained their structural morphology even after adsorption. The adsorption data were fitted to various kinetic and isotherm models to gain insights into the adsorption mechanism and behaviour. The pseudo-second-order kinetic model and Redlich–Peterson model best described the experimental data, indicating multi-layer adsorption and chemisorption as the predominant adsorption mechanism. The maximum adsorption capacity was determined to be 1128.46 mg g<sup>-1</sup> for MB and 387.6 mg g<sup>-1</sup> for MG, highlighting the high affinity of the carbon nanospheres towards cationic dyes. Moreover, CNS reusability and stability were examined through desorption and regeneration experiments, which revealed sustained efficiency over 7 cycles. CNSs were immobilised in a membrane matrix and examined for adsorption, which demonstrated acceptable efficiency values and opened the door for further improvement.

Received 26th March 2024  
Accepted 18th April 2024

DOI: 10.1039/d4na00254g

[rsc.li/nanoscale-advances](https://rsc.li/nanoscale-advances)

## Introduction

The textile industry is one of the largest in the world, yet wastewater discharged from it contains significant amounts of chemicals, toxic metals, and colours. If handled improperly, textile wastewater effluents, which are hazardous waste with poisonous complex components, can negatively impact the environment, compromising human health and marine ecosystems.<sup>1</sup> Due to the limited ability of these dyes to break

down naturally, the pollution generated by the textile dyeing sector remains long-lasting and cannot be concealed by the vivid hue of wastewater emissions.<sup>2</sup>

About 60 to 70% of the dyes used in the textile industry are azo dyes. Their interaction with the textile fiber and solubility in water are guaranteed by the presence of the main chromophore (–N=N–) group.<sup>3</sup> The two most often used cationic dyes in the textile industry are methylene blue (MB) and malachite green (MG). MG is a common cationic azo dye of the triphenyl-methane class, with a crystalline, green appearance and is water-soluble.<sup>4</sup> MG is frequently used in the colouring of paints, plastics, rubber, and other materials, as well as in the dyeing and printing of a range of natural and synthetic fibres.<sup>5,6</sup> Approximately 45–50% of the total production of industrial dyes is attributed to the reactive dye, MG.<sup>7</sup> However, it has been outlawed in several countries for aquaculture use due to its detrimental effects.<sup>8</sup> MB is a cationic thiazine dye that is widely used as a colourant, widely used for biological staining techniques, as well as for staining silk, wool, and cotton.<sup>9</sup> The

<sup>a</sup>Department of Chemistry, School of Sciences, CHRIST (Deemed to be University), Hosur Road, Bengaluru 560029, India. E-mail: murthyhegde@gmail.com

<sup>b</sup>Department of Chemistry, AMC Engineering College, Bannerghatta Road, Bengaluru 560083, India

<sup>c</sup>Centre for Advanced Research and Development (CARD), CHRIST (Deemed to be University), Hosur Road, Bengaluru 560029, India

<sup>d</sup>Department of Physics and Astronomy, College of Science, King Saud University, Riyadh 11451, Saudi Arabia

† Electronic supplementary information (ESI) available. See DOI: <https://doi.org/10.1039/d4na00254g>



marine ecosystem is severely impacted by the uncontrolled disposal of these dyes and auxiliary chemicals into water bodies.<sup>10</sup> Skin and eye irritation, nausea, breathing problems, vomiting, and diarrhoea are only a few adverse consequences of these dyes on human health.<sup>11</sup> In light of the importance of dye removal from wastewater streams, the quest for effective biogenic sorbents still has potential as a research topic.

Chemical oxidation, electrophoresis, ion exchange, chemical precipitation, photocatalysis, flocculation, membrane separation, and photocatalysis are some of the treatment methods used to eliminate organic contaminants from wastewater effluents.<sup>12,13</sup> However, the methods mentioned earlier come with various disadvantages, including ineffectiveness with low-concentration solutions, the generation of by-product sludge, and the need for subsequent treatment. Due to their substantial capacity for removing organic matter and affordability, adsorption techniques are highly effective in treating industrial wastewater.<sup>14</sup> Through considerable prior research<sup>12–18</sup> for treating textile and dye effluents, the efficacy of adsorption methods has been proven.

Carbonaceous adsorbents are generally prepared from different biomass and agricultural wastes due to their many benefits, including renewability, affordability of the precursor, and environmental friendliness.<sup>19</sup> Agricultural waste and biomass materials such as garlic peel,<sup>20</sup> areca nuts,<sup>18</sup> oil palm leaves,<sup>21</sup> onion peel,<sup>22</sup> etc., were frequently used as cost-effective biosorbents for eliminating cationic dyes by synthesizing CNSs from these precursors. Apart from these, a few other carbon materials derived from forestry residues, food processing waste, and agricultural waste are also used in dye removal applications such as oil palm fiber-based activated carbon,<sup>23</sup> watermelon peel biochar,<sup>24</sup> pea peel biochar,<sup>25</sup> mandarin peels,<sup>26</sup> carbon derived from neem bark,<sup>27</sup> raw walnut shell-based activated carbon,<sup>28</sup> groundnut shell powder, coconut coir powder and activated corn leaf carbon,<sup>29</sup> etc.

Moreover, biowaste-derived CNSs have distinct advantages as they provide a sustainable, environmentally friendly, and easy synthesis approach option that makes use of agricultural byproducts that would otherwise go to waste, as reported in earlier research.<sup>18–22</sup> Biomass-derived CNSs have inbuilt porosity being mesoporous in nature with spherical morphology, making them an ideal candidate for dye degradation applications. Furthermore, the renewable nature of biowaste provides a steady and plentiful supply, decreasing reliance on finite resources. Moreover, the use of biowaste-derived nanomaterials promotes circular economy concepts by transforming waste streams into value-added goods. Biowaste-derived CNSs frequently have distinct properties and functionalities, demonstrating their promise for not just effective and efficient water purification but also different applications. The adsorption capacity and surface characteristics of a bio-based adsorbent are impacted by factors such as the chemical activator utilized, the origin of the precursor material, and the method of activation. In this catalyst-free synthesis, the major role is played by the precursor material and the functionalities present in it. Generally, a good bio-adsorbent for removing dyes should meet the following criteria: high selectivity in a wide range of

concentrations, significant adsorption capacity for simple and complex samples, and other factors such as recyclability, quick desorption from the dye surface, and environmental friendliness.<sup>18,30</sup> All of the criteria are fulfilled by the CNSs synthesized from this biomass.

The current work investigated the dye removal efficacy of *Arachis hypogaea* (groundnut/peanut) biowaste-based novel nano-adsorbents for cationic dyes such as MB and MG under various parameters without any chemical modification. This is the first reported study on the synthesis of carbon nanospheres from groundnut skin. Groundnut is an oil plant that is widely farmed in China. China's groundnut production accounts for one-third of global total production. *Arachis hypogaea* shell is a plentiful and low-cost agricultural byproduct. However, most groundnut shells are either burned or discarded carelessly, which leads to pollution and a significant depletion of natural resources. According to a study, groundnut shells can be used as an excellent adsorbent to remove organic contaminants, dyes, and heavy metals from aqueous solutions.<sup>31</sup> However, the use of groundnut skin has yet to be investigated to date for these applications. The skin of *Arachis hypogaea* is found to possess 88% of the overall antioxidant activity and 30% of the extracted oil content. It contains a cellulose content of 40.5%, lignin content of 26.4%, and hemicellulose content of 14.7%.<sup>32</sup> Our study underscores the economic viability of harnessing agricultural waste-derived precursors, aligning with sustainability objectives through the utilization of renewable resources and minimal environmental impact, while also introducing a novel catalyst-free synthesis approach that achieves exceptional dye removal efficiency. Using this waste to wealth approach will minimize costs, which is one of the major goals, thereby using it for wastewater purification applications.

## Experimental

### Materials

The biowaste from *Arachis hypogaea* skin used to make the nanospheres was obtained from the Western Ghats. Methylene blue, malachite green, congo red, and indigo carmine dyes were procured from Sigma Aldrich Pvt. Ltd, sodium hydroxide (NaOH) was procured from CDH, and hydrochloric acid (HCl) was procured from Thomas Baker. Polysulfone (PSU), obtained as the base polymer from Sigma Aldrich, was employed in the preparation of the membrane. *N*-Methyl 2-pyrrolidone (NMP) was obtained from Finar Chemicals. The pyrolysis procedure was carried out in a tube furnace procured from NoPo Nanotechnologies, India. Using a pH meter (Labman Scientific Instruments), pH changes were monitored. A magnetic stirrer thoroughly mixed both the adsorbent and adsorbate in a beaker at the desired mixing speed. The dye solution that had been treated and the nanoparticles that had taken up the dye were separated using a microprocessor-based centrifuge. For the regeneration investigation, ethanol served as the solvent. Millipore distilled water was used for all of the studies. Acetone and water were used as solvents for cleaning and rinsing. A glass plate was used as the substrate for membrane casting.

## Synthesis

The synthesis of *Arachis hypogaea* skin-derived carbon nanoparticles requires grinding of the *Arachis hypogaea* skin to a coarse powder form using a mixer. Then the powder is sieved using 75  $\mu\text{m}$  mesh to obtain a homogeneous powder. The precursor powder is dried to eliminate any residual moisture within the powder. The carbonization of the precursor is carried out at 800  $^{\circ}\text{C}$  under a steady flow of nitrogen gas (150  $\text{mL cm}^{-3} \text{min}^{-1}$ ) in a quartz tube furnace. The resulting sample was labeled as Groundnut Skin-Carbon Nanospheres (GS-CNSs) and was then characterized.

## Characterisation

The absorbance of dyes was measured using a UV-Visible spectrophotometer. An FE-SEM from ThermoScientific- Apreo 2 S was used to characterize the surface morphology of the synthesised nanoparticles before and after the adsorption. Utilising a MiniFlex 600 from Rigaku Corporation, X-ray diffraction (XRD) patterns are used to assess the crystallinity of GS-CNSs. The Fourier transform infrared spectra (FTIR) technique using an IRSpirit-L, Shimadzu was used to identify the available functional group of raw groundnut skin powder and pyrolyzed GS-CNSs. Raman spectra were analysed using a Renishaw inVia Raman microscope for information about the crystalline structure. The determination of surface characteristics, such as pore dimensions, volume, and surface area, was accomplished using  $\text{N}_2$  adsorption-desorption isotherms measured with a BELSORP-max Microtrac instrument. The thermal stability of the precursor was tested by thermogravimetry analysis (TGA) using a PerkinElmer STA 6000. An optical profilometer was used for surface topology for membrane characterization.

## Batch adsorption experiments

Adsorption experiments were conducted by introducing 5 mg of GS-CNSs into a 10 mL dye solution with a native pH. The dye concentrations were determined using a UV-Vis spectrophotometer at 663 nm for MB and 614 nm for MG. Removal efficiency in the percentage of the nanoparticles was calculated using eqn (1):

$$\text{Removal efficiency (\%)} = \frac{C_0 - C_e}{C_0} \times 100 \quad (1)$$

where  $C_0$  and  $C_e$  are the dye concentrations under initial and equilibrium conditions in  $\text{mg L}^{-1}$ , respectively.

GS-CNSs were then employed to optimize contact time. To evaluate MB and MG dyes at a native pH, 5 mg of adsorbent was introduced into a 10 mL dye solution with a concentration of 10  $\text{mg L}^{-1}$ . For the purpose of adsorbent dosage optimization, 1, 3, and 5 mg of adsorbent were employed for 10 mL of a dye solution with a concentration of 10  $\text{mg L}^{-1}$  at native pH. Different pH dye solutions were tested further to determine the influence of pH on dye removal. For acidic pH, 1 N HCl solution was used, and for basic pH, a few drops of 1 M NaOH were added. Likewise, varying concentrations of 5, 10, and 15  $\text{mg L}^{-1}$  were prepared through dilution of the initial 50  $\text{mg L}^{-1}$  stock

solution to optimize the dye concentrations. These solutions were subjected to stirring at 300 revolutions per min (rpm) using a magnetic stirrer over various time intervals in separate experiments, followed by 10 min for centrifugation at 3000 rpm.

To gain insight into the adsorption mechanism, specifically the bonding interactions between the adsorbent molecules and the adsorbate, the Freundlich, Langmuir, Temkin, and Redlich-Peterson isotherms were investigated. Kinetic studies were carried out using pseudo first order and pseudo second order models. These isotherms were fitted using linear square fitting using the Origin Pro 9.0 64 bit software.

## Preparation of membranes

According to published research, diffusion-induced phase separation (DIPS) is used to obtain PSU-based flat sheet membranes. The casting solution of PSU was prepared by dissolving 4 g of PSU in 16 mL of NMP at 60  $^{\circ}\text{C}$ . After complete dissolution, 10 mg of GS-CNSs were added for dispersion to the viscous solution. The obtained homogeneous solution was stirred at 60  $^{\circ}\text{C}$  for 24 h. Subsequently, the solution was cast onto a pristine glass plate and submerged in a coagulation bath (water) overnight. After the phase inversion process had been completed, the membrane was carefully removed from the glass plate and subjected to multiple rinses with distilled water to thoroughly eliminate any remaining excess NMP.<sup>33</sup> The membrane was then dried and kept for further investigation.

## Results and discussion

### Synthesis of GS-CNSs

Pyrolysis method is used to produce carbon nanospheres because it efficiently transforms carbon-rich precursors into uniform, spherical carbon nanoparticles by breaking down the precursor molecules at high temperatures in the absence of oxygen. This method offers better control over particle size and composition, making it ideal for producing carbon nanospheres with desired properties for various applications. The initial stage, at around 100  $^{\circ}\text{C}$ , is where moisture's main evaporation occurs. Subsequently, hemicellulose undergoes rapid decomposition at elevated temperatures between 220  $^{\circ}\text{C}$  and 315  $^{\circ}\text{C}$ . Lignin, on the other hand, goes through pyrolysis over a broad temperature spectrum. Cellulose degradation primarily occurs between 315  $^{\circ}\text{C}$  and 400  $^{\circ}\text{C}$ . All volatile substances, including heteroatoms such as  $\text{CO}_2$ ,  $\text{CH}_4$ ,  $\text{CO}$ , and certain organic compounds, are eliminated during carbonisation. Consequently, most of the remaining solid residue is carbonaceous in nature.<sup>34</sup>

### Characterization

**FESEM-EDS.** The elemental composition and surface topography of the sample were assessed through field emission scanning electron microscopy and energy dispersive X-ray spectroscopy (FESEM-EDS) analysis. The morphological characteristics of the carbon residues gathered align with the typical features observed in the pyrolysis synthesis technique

employed.<sup>35</sup> The FESEM image of the pyrolysis of biomass shows unique solid structures, which are seen in GS-CNSs.

Fig. 1a confirms the spherical nature of the nanosphere synthesized with a uniform size of 20–70 nm. Instead of being distinct entities, the GS-CNSs seem to be present as a cluster of spheres which helps in dye removal. The aggregation of the spherical particles may have resulted from prolonged reaction durations and controlled cooling from synthesis temperature to room temperature. Fig. 1b shows that the spherical nature is intact even after dye adsorption. After adsorption, the homogeneous morphology and elimination of pores in the FESEM images of the GS-CNSs indicated that the surface had been covered by dye molecules that had adhered to the pores. The GS-CNSs's carbon content was as high as 77.96% before adsorption, according to the EDS of the GS-CNSs, and it remained at roughly 75.64% even after adsorption.

**XRD.** XRD (X-ray diffraction) is a crucial tool in solid-state chemistry and materials science used to elucidate the structural arrangement of materials. The presence of two distinct diffraction peaks ( $2\theta = 23^\circ$  and  $42^\circ$ ) in the XRD pattern which correspond to the (002) and (101) planes can be attributed to the graphitic nature and the formation of highly organized carbon nanospheres (Fig. 1c). This can also be confirmed in the literature,<sup>36</sup> where the authors have characterized groundnut shell derived carbon nanospheres.

**Raman spectroscopy.** The use of Raman spectroscopy to demonstrate the formation of carbon nanospheres is another valuable method. The accumulated carbon structure abnormalities can be identified by the presence of a D-band which appears at  $1347\text{ cm}^{-1}$ . The production of  $\text{sp}^2$  hybridized  $\text{C}=\text{C}$  bonds in the G-band at  $1600\text{ cm}^{-1}$  (Fig. 1d) indicates the graphitic nature of the resulting carbon nanospheres. In recent literature,<sup>37</sup> this structure can be confirmed. The D-band peak to G-band peak intensity ratio is integralised to determine the degree of disorder in carbon ( $I_D/I_G$ ). The  $I_D/I_G$  ratio of GS-CNSs was calculated to be 1.11 before adsorption and 0.89 after

adsorption, which confirms the relatively high level of disorder structural defects of the synthesized nanospheres. The decrease in the  $I_D/I_G$  ratio might suggest that the dye molecules have adsorbed onto the surface of the nanoparticles and influenced their structural properties. This can happen through pi-pi stacking interactions, van der Waals forces, or other chemical interactions between the dye molecules and the GS-CNSs.

**BET.** Brunauer–Emmett–Teller (BET) analysis provided critical insights into the structural characteristics of GS-CNSs. The results revealed a total pore volume of  $0.1284\text{ cm}^3\text{ g}^{-1}$ , signifying the capacity of the material to accommodate gases or liquids within its porous framework. Moreover, the mean pore diameter, which was determined to be 2.90 nm, highlighted the mesoporous size of these pores. The isotherm profiles exhibit a resemblance to Type IVa, suggesting a mesoporous characteristic (Fig. 2b). In a Type IVa isotherm, capillary condensation takes place, accompanied by hysteresis phenomena. Particularly noteworthy is the presence of a distinct H4-type loop, which signifies the existence of relatively narrow mesopores. To ascertain the distribution of pore sizes, the modified Kelvin equation, as developed by Barrett, Joyner, and Halenda and referred to as the BJH method, was utilized. The analysis yielded a pore size measurement of 2.43 nm, as illustrated in Fig. 2a. The specific surface area, a pivotal parameter in understanding the material's reactivity and adsorption capabilities, was found to be  $177.08\text{ m}^2\text{ g}^{-1}$ . The mean pore diameter, surface area, and pore size collectively confirm the mesoporous nature and, thereby, the presence of active sites on the surface of the nanospheres so that adsorption can happen. These BET findings collectively also underscore the material's promising potential for various applications, where its porous nature and substantial surface area can play a vital role.

**TGA.** Thermogravimetric analysis (TGA) was carried out for the precursor to understand the characteristic decomposition pattern wherein the precursor was subjected to heating from 30 to  $800\text{ }^\circ\text{C}$  at  $10\text{ }^\circ\text{C min}^{-1}$  under a nitrogen atmosphere using a PerkinElmer STA 6000. As depicted in Fig. 2c, the TGA plot might be interpreted as the culmination of three decomposition processes. In stage 1, weight loss ( $\sim 10\%$ ) occurs at temperatures below  $200\text{ }^\circ\text{C}$  due to moisture and water content removal from the precursor. The raw material lost the majority of its weight ( $\sim 65\%$ ) during stage 2, which involved increasing the temperature from around  $200$  to  $550\text{ }^\circ\text{C}$ . This is due to the elimination of lignocellulosic components as volatile gasses from the precursor matrix. Beyond  $550\text{ }^\circ\text{C}$ , there was little change in weight, showing carbon enrichment due to the elimination of volatile chemicals at high temperatures, indicating stability in stage 3. Thereby, carbonisation at a higher temperature of  $800\text{ }^\circ\text{C}$  was performed to obtain the pure carbon material.

**Zeta potential.** The surface charge of GS-CNSs was found to be  $-19.2\text{ mV}$ , indicating a primarily negative charge [refer to the ESI for Fig. S1†]. The negative charge can be attributed to the  $\pi$ - $\pi$  interactions between the graphitic structures of GS-CNSs. The presence of active adsorbent sites on the surface of the nanospheres is due to this phenomenon of charge and the mesoporous nature of the nanospheres. This negative surface charge

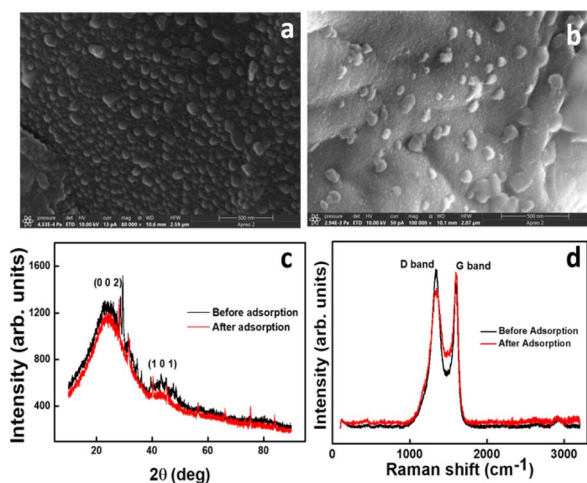


Fig. 1 SEM image of GS-CNSs (a) before adsorption and (b) after dye adsorption; (c) XRD patterns and (d) Raman spectra of GS-CNSs before and after dye adsorption.

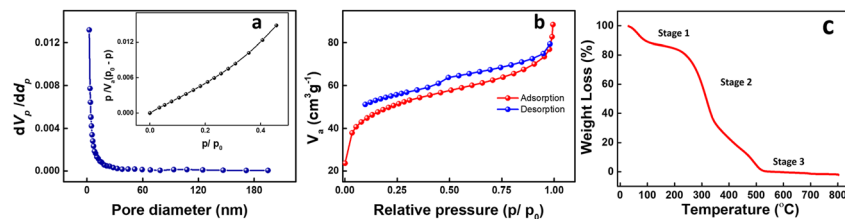


Fig. 2 (a) BJH pore size distribution plot; (b)  $N_2$  adsorption–desorption isotherm for GS-CNSs; (c) TGA curve for raw precursors.

can cause repulsion or electrostatic interactions with similarly charged species, such as anionic dyes, limiting their adsorption or interaction with nanoparticles. However, the same negative charge can aid in the interaction with cationic dyes, which normally have a positive charge. The electrostatic attraction between the negatively charged GS-CNSs and the positively charged cationic dyes promotes their adsorption onto the surface of the nanoparticles, resulting in faster degradation or removal from the solution. In contrast, anionic dyes, which have a negative charge, may experience electrostatic repulsion from negatively charged nanoparticles, resulting in restricted contact and degrading efficiency. In addition, the CNSs derived from biomass have the distinct features of stability, sustainability, and selectivity.

**FTIR.** The FTIR spectra of the raw precursor and GS-CNSs after pyrolysis are presented in Fig. 3. The broad peak observed at  $3340\text{ cm}^{-1}$  is indicative of the  $-\text{OH}$  group functionality present in the groundnut skin. Additionally, lignocellulosic components' aromatic  $\text{C}-\text{H}$  bond stretching vibrations at a frequency of  $2900\text{ cm}^{-1}$  can be observed. The peak at  $2420\text{ cm}^{-1}$  confirms the presence of  $\text{O}=\text{C}=\text{O}$  stretching in the precursor. A peak at  $2238\text{ cm}^{-1}$  shows an alkyne moiety in the precursor since it has cellulose and lignin. The peaks at  $2021\text{ cm}^{-1}$  and  $1912\text{ cm}^{-1}$  confirm the presence of the allene group. The peak at  $1747\text{ cm}^{-1}$  confirms the  $\text{C}=\text{O}$  stretching of

the  $\text{COOH}$  group in hemicellulose and lignin present in the *Arachis hypogaea* powder. Due to lignin's conjugated carbonyl and the hemicelluloses in the groundnut, there is a stretching vibration at  $1627\text{ cm}^{-1}$ . The peak at  $1435\text{ cm}^{-1}$  corresponds to the bending of  $\text{C}-\text{H}$  bonds in the methyl group of lignin.

A characteristic feature of cellulose and hemicellulose is the symmetric deformation of  $\text{C}-\text{H}$  aldehyde bending, which is observable at  $1390\text{ cm}^{-1}$ . The  $1244\text{ cm}^{-1}$  peak shows aromatic ester  $\text{C}-\text{O}$  stretching for a lignocellulosic nature. The peaks observed in the spectral range of  $1000\text{--}1175\text{ cm}^{-1}$  and  $900\text{--}550\text{ cm}^{-1}$  correspond to the stretching and non-symmetrical bending deformations involving  $\text{C}-\text{O}$ ,  $\text{C}-\text{C}$ , and  $\text{C}-\text{O}-\text{C}$  bonds, as well as vibrations associated with  $\text{C}-\text{H}$  bonds, all of which are linked to the presence of cellulose and hemicellulose. Thus, FTIR data show that hemicellulose and lignocellulose are the main components of biowaste that can serve as carbon precursors in the production of highly ordered carbon nanospheres.<sup>18,36,38</sup> After pyrolysis, the lignocellulosic group has been converted to carbon. The peak at  $1800\text{ cm}^{-1}$  and  $1450\text{ cm}^{-1}$  indicates the occurrence of  $\text{C}=\text{O}$  stretching and  $\text{C}-\text{H}$  bending, respectively, showcasing that the precursor is pyrolysed.

### Adsorption studies

**Effect of contact time.** The impact of contact time on the adsorption of MB and MG dyes was investigated with GS-CNSs (Fig. 4a and b). The acquired results demonstrate that GS-

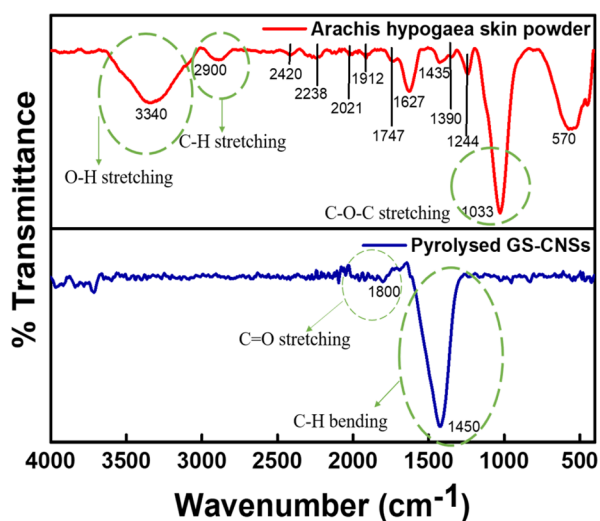


Fig. 3 FTIR analysis of raw *Arachis hypogaea* skin powder and pyrolysed GS-CNSs.

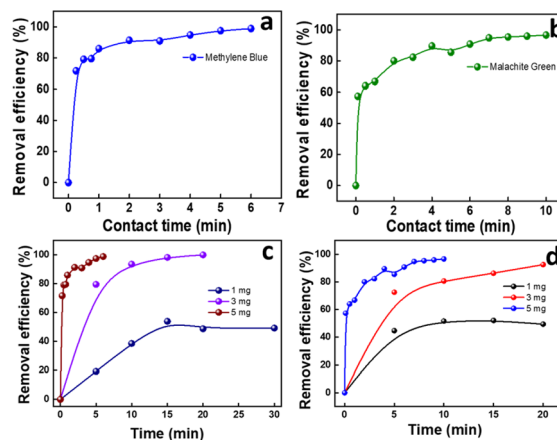


Fig. 4 Effect of contact time for GS-CNSs on (a) MB and (b) MG dyes; effect of GS-CNS dosage on (c) MB and (d) MG dye adsorption.

CNSs effectively adsorbed both model dyes in under five min, showing a removal efficiency of 97.48% for MB and 85.53% for MG. As the contact time increased, the removal efficiency exhibited a gradual increase, reaching a level of 96.6% for MG within a 10-min timeframe (Fig. 4b) and 98.84% for MB in 6-min timeframe (Fig. 4a). The availability of vacant adsorption sites caused the initial constant increase. Further time increments, however, did not impact the removal effectiveness because they prevented subsequent ions from profoundly entering into the adsorbent molecular structure as dye molecules accumulated on all accessible adsorption sites.<sup>18,39</sup> Additionally, the desorption of dyes was negligible once equilibrium was reached, showcasing the robustness of the adsorption process and affirming the applicability of GS-CNSs for scaling up to larger operations.

A comparative study is tabulated in Table 1 to demonstrate the effectiveness of the present work with respect to the previously conducted research and its results for cationic dye removal using carbon nanospheres as adsorbents.

**Effect of GS-CNS dosage.** By adjusting the dosage of GS-CNSs while maintaining the amounts of all other components constant, the effect of GS-CNS dose on the removal of MB and MG dyes was investigated. Fig. 4c shows the removal efficiency of MB for 1, 3, and 5 mg dosage of adsorbent. It is evident from the plots that when the dosage of the adsorbent is increased, the removal efficiency of the dye also increases.

For MB, the removal efficiency was nearly 19, 80, and 98% for 1, 3, and 5 mg, respectively, by keeping the contact time at 5 min. Within 2 min, the efficiency was 91.3% for 5 mg adsorbent dosage. It is obvious that GS-CNSs can remove 99% of the methylene blue dye regardless of dosage; however, smaller dosages will require a longer time. Additionally, it's possible that greater dosages will result in more open adsorbent sites and surface area, which will make it easier for dye molecules to bind to the surface.<sup>40</sup>

The removal efficiency of MG for doses of 1, 3, and 5 mg is each depicted in Fig. 4d. For MG, the removal efficiency was 44, 74, and 85% for 1, 3, and 5 mg, respectively, by keeping the contact time at 5 min. For the 3 mg dosage, the removal efficiency crossed 92% after 20 min, whereas for the 5 mg dosage, it

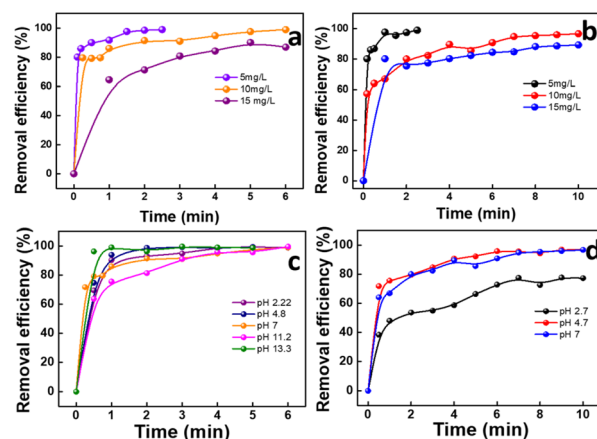


Fig. 5 Effect of (a) MB and (b) MG dye concentration on GS-CNSs; effect of pH on (c) MB and (d) MG dye adsorption with GS-CNSs.

reached 96.6% in just 10 min. It must also be noted that the efficiency reached 80% within 2 min. Because of this, the dosage of 5 mg of GS-CNSs was decided upon for further investigations.

In addition, anionic dyes (such as congo red and indigo carmine) were tested in order to test the feasibility, but the removal efficiency was low even after a longer duration. Indigo carmine resulted in 12% removal in 5 minutes with a 3 mg dosage of GS-CNSs, whereas congo red showed 14% removal with the same GS-CNS dosage and time for 10 mg L<sup>-1</sup> dye solution [refer to ESI Fig. S2† for dye removal studies for anionic dyes]. On the other hand, the cationic dyes MB and MG showed around 80% and 74% removal, with a 3 mg dosage of GS-CNSs in 5 minutes. This also contributes to the selectivity and surface charge on the carbon nanospheres, due to which a higher removal efficiency of cationic dyes can be observed than anionic dyes. Electrostatic stabilization plays a vital role here.

**Effect of initial dye concentration.** The quantity of dye molecules and the number of available adsorbing sites play key roles in determining the ability of the adsorbent to absorb substances. Fig. 5a for MB and 5b for MG depict the results of the dye concentration influence on the removal process.

Table 1 Comparative data for removal of cationic dyes using other bio-adsorbents in the literature at native pH

Dye	Dye conc. (μM)	CNS dosage (mg)	Adsorbent used & synthesis method	Removal efficiency (%)	Time (min)	Adsorption isotherm & kinetics	Ref
Malachite green	10	1	CNSs derived from oil palm leaves; pyrolysis at 1000 °C	90	10	Temkin isotherm; pseudo second order	21
Brilliant green	10	1	CNSs derived from oil palm leaves; pyrolysis at 1000 °C	99	10	Freundlich; pseudo second order	21
Malachite green	10	1.5	Garlic peel based mesoporous CNSs; pyrolysis at 1000 °C	98.9	70	Langmuir; pseudo second order	20
Methylene blue	10	1.5	Porous areca nut CNSs; pyrolysis at 1000 °C	99	70	Langmuir; pseudo second order	18
Methylene blue	15.63	5	<i>Arachis hypogea</i> skin derived CNSs; pyrolysis at 800 °C	98.4	2	R-P; pseudo second order	This work
Methylene blue	31.26	5	<i>Arachis hypogea</i> skin derived CNSs; pyrolysis at 800 °C	98.8	6	R-P; pseudo second order	This work
Malachite green	13.70	5	<i>Arachis hypogea</i> skin derived CNSs; pyrolysis at 800 °C	97.4	2	R-P; pseudo second order	This work
Malachite green	27.40	5	<i>Arachis hypogea</i> skin derived CNSs; pyrolysis at 800 °C	96.6	10	R-P; pseudo second order	This work

For MB, 5, 10, and 15 mg L<sup>-1</sup> dye concentrations were used with 5 mg of adsorbent dosage for the experiment. For 5 mg L<sup>-1</sup> (15.63 μM), the efficiency reached 98.4% in just 2 min. Similarly, for 10 mg L<sup>-1</sup> (31.26 μM) and 15 mg L<sup>-1</sup> (46.9 μM) concentrations, the efficiency was 98.8% and 86.81%, respectively in 6 min.

For MG, the 5 mg L<sup>-1</sup> (13.70 μM) dye concentration showed 97.4% removal in merely 2 min, as depicted in Fig. 5b. When investigated for 10 mg L<sup>-1</sup> (27.40 μM) and 15 mg L<sup>-1</sup> (41.11 μM) dye concentrations, the dye removal efficiency was 96.61 and 89.24%, respectively, in 10 min. It is evident from the provided data for both the dyes that at lower concentrations, adsorption occurs at a higher pace, which is attributed to a smaller ratio of dye molecules to active adsorbent sites at lower concentrations. However, as the concentration increases, this ratio increases, leading to the saturation of the pores. During this saturation stage, the efficiency of dye removal decreases as dye molecules start to compete with each other for binding to the inner pores of the adsorbent.<sup>41</sup> The critical variables influencing the retarding adsorption process are hence the optimal concentration and the growing ion competition that results in the saturation of active adsorption sites when dealing with higher initial concentrations. The reduced adsorption rate at higher concentrations can also be caused by the repulsion between adsorbed and remaining dye molecules.<sup>18,42</sup>

**Effect of pH.** Studies on pH were conducted in an acidic, alkaline, and native pH environment. The pH of the solution plays a substantial role in influencing the dye structure, altering the surface charge of the adsorbent and affecting the degree of ionization of dyes, primarily as a result of the competitive interactions involving hydrogen ions. Variations in pH can directly influence the physicochemical properties.<sup>43</sup> For MB, the removal efficiency was >95% under all the pH conditions, showing effective dye removal within 5 min, as shown in Fig. 5c. The effectiveness of MB at lower pH levels can be attributed to protonation, which leads to the creation of positive charges on the surface of the adsorbent. This, in turn, causes competition for adsorption sites between the cationic dye and additional H<sup>+</sup> ions. Conversely, at higher pH levels, the greater presence of OH<sup>-</sup> ions enhances the electrostatic attraction between the adsorbent's surface and the cationic dye, thereby increasing efficiency under alkaline conditions.<sup>44</sup>

For MG dye, the efficiency was better at native and slightly acidic pH. Within 10 min of contact time, the efficiency of dye removal was found to be 96.6% at both pH 4.7 and pH 7 though it dropped to 77.18% at pH 2.72, as indicated in Fig. 5d. At a highly basic pH, the dye turns cyan and then colourless when saturated NaOH solution is added to the dye solution. Under low pH conditions, the abundance of readily available H<sup>+</sup> ions can result in the protonation of electron-rich sites on the contaminants and/or CNSs. However, contaminants may compete with the OH<sup>-</sup> availability for basic pH for the sorbent's adsorption sites.<sup>45</sup> Because MG is known to exist in cationic form in aqueous environments, it is attracted to negatively charged surfaces. The adsorption of MG was enhanced at higher pH values until 7 and subsequently reduced as the pH increased. This behaviour may be explained by the presence of

extra negative charges on the nanoparticles' surfaces, which might strengthen their electrostatic interaction with the cationic dye MG.<sup>46</sup> Due to the transformation of MG into protonated MG (MGH) under acidic pH conditions and into a carbinol base under basic pH conditions, the structural modifications of the molecule should be taken into consideration when removing the compound.<sup>47</sup>

### Adsorption isotherms

The relationship between the quantity of adsorbate adsorbed onto a particular adsorbent surface and the equilibrium concentration of the substrate while in contact with the adsorbent under constant temperature conditions is shown by adsorption isotherm curves.<sup>48,49</sup> The Langmuir, Freundlich, Temkin, and Redlich–Peterson models were utilized in the current work to understand the adsorption mechanism and to linearly fit the batch equilibrium data.

**Langmuir isotherm.** The Langmuir adsorption model, originally formulated for the study of gas–solid phase adsorption, has now found application in assessing and contrasting the adsorption capacities of different adsorbents. It accomplishes this by considering surface covering through the establishment of a dynamic equilibrium between the rates of adsorption and desorption. The extent of open surface area on the adsorbent exhibits an inverse relationship with adsorption, whereas the degree of surface coverage is inversely associated with desorption.<sup>50</sup>

The following linear form can be used to express the Langmuir eqn (2):<sup>51</sup>

$$\frac{C_e}{q_e} = \frac{1}{q_m K_L} + \frac{C_e}{q_m} \quad (2)$$

where  $q_m$  (mg g<sup>-1</sup>) is the adsorbent's monolayer sorption capacity and  $C_e$  (mg g<sup>-1</sup>) is the equilibrium adsorbate concentration. The adsorption capacity is measured using the Langmuir constant,  $K_L$  (mg g<sup>-1</sup>), which is related to variations in the porosity and surface area of the adsorbent. This implies that an increased adsorption capacity can be anticipated when both the surface area and pore volume are greater.

This also implies the existence of homogeneous energy surface sites where adsorption occurs, as indicated by the initial

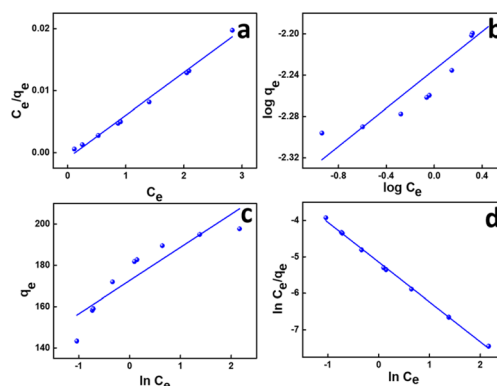


Fig. 6 (a) Langmuir, (b) Freundlich, (c) Temkin, and (d) Redlich–Peterson isotherms of MB adsorption.

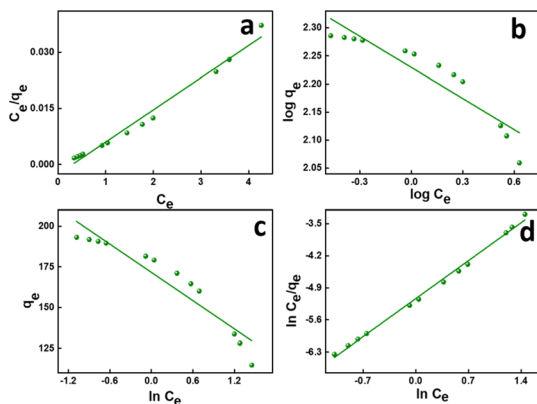


Fig. 7 (a) Langmuir, (b) Freundlich, (c) Temkin, and (d) Redlich-Peterson isotherms of MG adsorption.

increase in the curve and the achievement of the  $n$ -equilibrium point.<sup>49</sup> As shown in Fig. 6a for methylene blue and Fig. 7a for malachite green, the graph is plotted with  $C_e/q_e$  on the  $y$ -axis against  $C_e$  on the  $x$ -axis. From the plotted graph, the regression coefficient obtained for MB was 0.9905, and for MG, it was 0.9810, showing that MB adsorption best fits this isotherm. After calculations, the maximum adsorbent capacity for MB and MG was  $1128.46 \text{ mg g}^{-1}$  and  $387.6 \text{ mg g}^{-1}$ , respectively. The  $R_L$  parameter signifies that adsorption is non-reversible when  $R_L = 0$ , linear when  $R_L = 1$ , unfavourable when  $R_L > 1$ , and favourable when  $R_L$  falls within the range of 0 to 1. Here, for both MB and MG adsorption, the  $R_L$  is favourable since the values obtained were 0.43 and 0.25, respectively.

The Langmuir model is grounded on the concept that the adsorption occurs through monolayer adsorption on a uniformly structured adsorbent surface. There are only a few identical adsorbate-binding sites. Additionally, adsorbed molecules do not come into contact with one another.

**Freundlich isotherm.** On heterogeneous surfaces, adsorption processes can be described using this isotherm.<sup>52</sup> It offers an equation for both the exponential distribution of active sites and their corresponding energies as well as surface heterogeneity in the adsorption process. The following eqn (3) is the linear form of the Freundlich isotherm:<sup>51</sup>

$$\log q_e = \log K_F + \frac{1}{n} \log C_e \quad (3)$$

where adsorption capacity is shown by  $K_F$  ( $\text{L mg}^{-1}$ ) and adsorption intensity is indicated by  $1/n$ . The value of  $n$  between 0 and 10 implies favourable adsorption, and these parameters are established through data fitting. The obtained  $n$  value for MB is 10.79 and for MG is 5.41, confirming the favourable adsorption.

**Temkin.** The Temkin isotherm model accounts for the influence of indirect interactions between adsorbate molecules on the adsorption process. Additionally, it assumes that the heat of adsorption for each molecule in the adsorbed layer decreases linearly as the surface coverage increases. The Temkin isotherm can only operate at intermediate ion concentrations.<sup>53</sup> The following linear eqn (4) represents the Temkin isotherm model:<sup>51</sup>

$$q_e = \frac{RT}{b} \ln K_T + \frac{RT}{b} \ln C_e \quad (4)$$

where  $b$  is the Temkin constant related to the heat of sorption ( $\text{J mol}^{-1}$ ),  $K_T$  ( $\text{L g}^{-1}$ ) is the Temkin isotherm equilibrium binding constant,  $C_e$  ( $\text{mg L}^{-1}$ ) is the concentration of dye molecules at equilibrium,  $q_e$  ( $\text{mg g}^{-1}$ ) is the quantity of dye molecules removed at equilibrium,  $R$  is the universal gas constant ( $8.314 \text{ J mol}^{-1} \text{ K}^{-1}$ ), and  $T$  is the temperature (298 K). The constants are determined by plotting the quantity absorbed,  $q_e$  vs.  $\ln C_e$ ,<sup>20,54</sup> as shown in Fig. 6c and 7c for MB and MG, respectively, and the values obtained from the graph are tabulated in Table 2. The Temkin graph indicates a regression coefficient fit of  $R^2 = 0.8163$  and  $0.8905$  for MB and MG, respectively. As a result,  $K_T = 1.09764 \text{ L g}^{-1}$  for MB. Similarly,  $B_T = R_T/b = 1.608 \text{ J mol}^{-1}$  for MB and  $-0.03107 \text{ J mol}^{-1}$  for MG show that the adsorption process is exothermic and physical in nature.

**Redlich-Peterson.** The Redlich-Peterson isotherm forms when the Langmuir and Freundlich isotherms are combined. Advantageously, the numerator of the Langmuir isotherm is nearer to the Henry area at infinite dilution.<sup>51</sup> This empirical isotherm model has three parameters. The adsorption process is consequently a combination and deviates from ideal monolayer adsorption because it contains components from both the Langmuir and Freundlich equations.<sup>55</sup> The linear form of the model is given in eqn (5):

$$\ln \frac{C_e}{q_e} = B \ln C_e - \ln A \quad (5)$$

where  $q_e$  ( $\text{mg g}^{-1}$ ) represents the quantity of the adsorbate in the adsorbent at equilibrium,  $C_e$  ( $\text{mg L}^{-1}$ ) represents the equilibrium concentration,  $B$  is the Redlich-Peterson parameter, and  $A$  is the Redlich-Peterson isotherm constant.<sup>49</sup> In the graph between  $\ln C_e/q_e$  vs.  $\ln C_e$  and the accompanying Fig. 6d and 7d for MB ( $R^2 = 0.9980$ ) and MG ( $R^2 = 0.9980$ ) dyes, the corresponding values are tabulated in Table 2, which best fit this isotherm. The Redlich-Peterson parameter was calculated to be  $-1.09269$  for MB, whereas for MG, it was  $2.72789$ . This isotherm model is versatile and can be applied to both homogeneous and heterogeneous systems. It captures adsorption equilibrium by

Table 2 Summary of isotherm constants and correlation coefficients for MB and MG dyes on GS-CNS adsorption studies

Isotherm models	Parameters	Methylene blue	Malachite green
Langmuir	$q_m$ ( $\text{mg g}^{-1}$ )	1128.46	387.6
	$K_L$ ( $\text{L g}^{-1}$ )	0.13	0.3
	$R_L$	0.43	0.25
	$R^2$	0.99054	0.98101
Freundlich	$K_F$	0.11	9.3
	$n_F$	10.79	5.41
	$R^2$	0.78257	0.84777
Temkin	$B_T$	1.608	$-0.03107$
	$K_T$	1.09764	—
	$R^2$	0.81634	0.89053
Redlich-Peterson	$B$	$-1.09269$	2.72789
	$A$	169.824	169.43
	$R^2$	0.99807	0.99572



**Table 3** Summary of kinetic model constants for MB and MG dye adsorption studies

Kinetic models		Methylene blue	Malachite green
PFO	$k_1$ ( $\text{min}^{-1}$ )	0.0465206	0.0467048
	$q_e$ ( $\text{mg g}^{-1}$ )	65.831	61.384
	$R^2$	0.7805	0.77936
PSO	$k_2$ ( $\text{g mg}^{-1} \text{min}^{-1}$ )	0.000285	0.0001176
	$q_e$ ( $\text{mg g}^{-1}$ )	20063.6	19889.53
	$R^2$	0.99876	0.99678

exhibiting a linear relationship between a concentration in the numerator and an exponential function in the denominator, making it suitable for a broad spectrum of adsorbate concentrations.<sup>56</sup>

The experimental data show a strong fit for the Redlich–Peterson isotherm model, demonstrating its usefulness in predicting the adsorption behavior found in our study. The Redlich–Peterson model combines the Langmuir and Freundlich isotherm equations, providing a versatile method for characterizing adsorption on heterogeneous surfaces. It takes into account both monolayer and multilayer adsorption, allowing for differences in surface heterogeneity and adsorbate–adsorbent interactions. This complete model sheds light on the adsorption mechanisms that govern the interaction between GS-CNSs and the dye, helping in better understanding of the underlying processes that drive adsorption events.

### Adsorption kinetics

Adsorption kinetics determines the rate of uptake of an adsorbate over time at a particular concentration and offers details on adsorbate diffusion into the pores, indicating a likely sorption process. It aids in comprehending ideal circumstances and how changes in various adsorption factors impact rates.<sup>48,57</sup> The parameters and the corresponding values with the regression coefficient for the two kinetic models studied are tabulated in Table 3.

**Pseudo-first order.** Understanding the adsorption rate using Lagergren pseudo-first-order (PFO) kinetics is helpful for a wide range of contact times.<sup>54</sup>

This model is given in eqn (6):<sup>58</sup>

$$\log(q_e - q_t) = \log q_e - \frac{K_1 t}{2.303} \quad (6)$$

The amount of adsorbate in the adsorbent at equilibrium and time  $t$  (min), respectively, is represented by the variables  $q_e$  and  $q_t$  ( $\text{mg g}^{-1}$ ).  $k_1$  ( $\text{min}^{-1}$ ) is the pseudo-first-order rate constant in this equation. As a result of this characteristic, it is convenient to create a plot of  $\log(q_e - q_t)$  on the  $y$ -axis and contact time  $t$  on the  $x$ -axis, which is displayed in Fig. 8a and c for MB ( $R^2 = 0.7805$ ) and MG ( $R^2 = 0.77936$ ), respectively, to test this isotherm. The values are shown in Table 3  $k_1$  values for MB were found to be  $0.0465206 \text{ min}^{-1}$ , whereas for MG, it was  $0.0467048 \text{ min}^{-1}$ .

**Pseudo-second order.** According to the pseudo-second order (PSO) kinetics, adsorption occurs on two surface sites.<sup>49</sup> The below eqn (7) provides the pseudo-second order kinetic model's linear version:<sup>58,59</sup>

$$\frac{1}{q_t} = \frac{1}{K_2 q_e^2} + \frac{1}{q_e} t \quad (7)$$

where  $k_2$  ( $\text{min}^{-1}$ ) is the PSO rate constant and  $q_t$  and  $q_e$  ( $\text{mg g}^{-1}$ ) is the quantity of the adsorbate in the adsorbent at time  $t$  (min) and equilibrium, respectively. Therefore, plotting  $t/q_t$  on the  $y$ -axis with contact time  $t$  on the  $x$ -axis and taking note of the  $R^2$  coefficient of determination is appropriate, as shown in Fig. 8b and d for MB ( $R^2 = 0.99876$ ) and MG ( $R^2 = 0.99678$ ), respectively, in order to test this isotherm. This isotherm fits the adsorption to the maximum, confirming that the process is primarily chemical sorption and not physical sorption, as shown by the values from Table 3.

This suggests that the rate-limiting step of the adsorption process involves the interaction between the adsorbate molecules and the active sites on the adsorbent surface. This implies that the adsorption is controlled by the availability of active sites and the chemical affinity between the adsorbate and

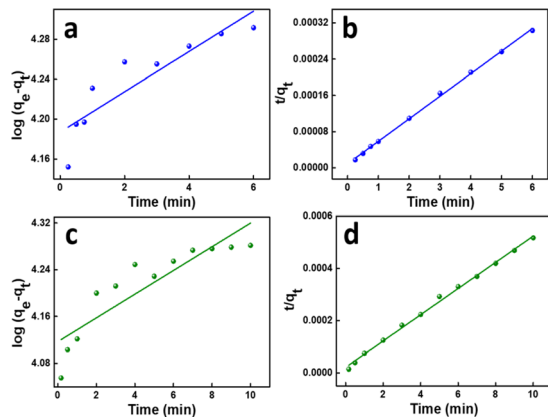


**Fig. 8** Pseudo first order kinetics for (a) MB and (c) MG; pseudo second order kinetics for (b) MB (d) MG adsorption.

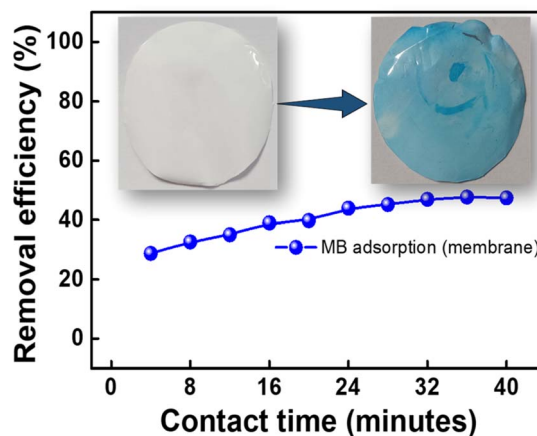


**Fig. 9** Removal efficiency of MB using a polysulfone membrane with GS-CNSs.

adsorbent. This kinetics is indicative of a heterogeneous adsorbent surface, where different active sites have different affinities for the adsorbate.

In conclusion, the experimental data demonstrate a strong fit to the PSO kinetic model as seen from the data provided in Table 3, indicating the adsorption of dyes onto GS-CNSs. This model suggests that the rate-limiting step in the adsorption process involves chemisorption, wherein the interaction between dye molecules and GS-CNSs occurs through strong chemical bonding. The superior fit of the PSO model emphasizes the importance of chemical interactions in driving the adsorption behavior of GS-CNSs, providing useful insights for the design and optimization of adsorption processes in a variety of applications.

**Membrane studies.** The membrane-based method employed in this study exhibited a removal efficiency of 48% for MB dye [dye conc:  $10 \text{ mg L}^{-1}$ , GS-CNS dosage:  $10 \text{ mg}$  ( $0.048 \text{ wt}\%$ )] within a relatively short duration of 36 min, as seen in Fig. 9. Although the bare membrane shows a removal efficiency of 10% in the same time-frame which is indicative that the GS-CNS embedded membrane shows better adsorption which can be optimized for further studies and explored. The obtained removal efficiency demonstrates the potential of membranes as a viable approach for the removal of cationic dyes from aqueous solutions. The removal rate in this study suggests the membrane's high adsorption capacity and efficient mass transfer properties, contributing to the effective removal of MB dye.

A homogeneous membrane structure without significant irregularities or surface variations for pure polysulfone membranes can be observed when viewed under an optical profilometer. This suggests that the membrane fabrication process using NMP has resulted in a high-quality and well-formed polysulfone membrane with consistent surface morphology. [Refer to the ESI for Fig. S3 and S4†].

The 2D and 3D optical profilometer image of the polysulfone membrane incorporating GS-CNSs exhibits a modified surface topography compared to the pure polysulfone membrane. The image reveals the presence of carbon nanospheres dispersed

throughout the membrane, leading to slight surface roughness and variations. This indicates the successful incorporation of the carbon nanospheres into the polysulfone matrix.

The optical profilometer image of the membrane after dye removal reveals significant changes in its surface topography. Prior to dye adsorption, the membrane exhibited a relatively smooth and uniform surface. However, following the adsorption process, distinct variations in the surface morphology are observed. The image displays irregularities, including localized depressions and roughness, indicating dye molecules being adsorbed onto the membrane surface. These alterations in the surface topography suggest that the dye molecules have effectively interacted and adhered to the membrane matrix. The optical profilometer image provides visual evidence of the successful dye removal process and highlights the membrane's ability to capture and retain cationic dyes from aqueous solutions.

**Reusability of the spent adsorbent.** Reusing synthesized adsorbents is necessary to reduce expenses and protect the environment. To achieve the objective of recycling the adsorbent, investigations were conducted to assess the desorption of the adsorbed dye and the potential reuse of the spent adsorbent in subsequent cycles. The first cycle's recovered nanoparticles were thoroughly cleaned with ethanol until the colouration was completely gone. After drying, it was used for a second cycle. Studies with MB dye up to 7 cycles were successfully carried out by similarly repeating the procedure. Over 97% removal efficiency was noted (Fig. 10). With more adsorbent recovery cycles, the adsorption effectiveness in the cycles gradually declines. For the 7th cycle, the removal efficiency slightly declined to 90%. The marginal reduction in pollutant removal efficiency could be attributed to the depletion of the adsorbent material following each cycle of adsorption and recovery, a decrease in the availability of adsorption sites, and the obstruction of openings or pores.<sup>60</sup>

## Conclusions and outlook

In the present study, *Arachis hypogaea* skin-derived carbon nanospheres are used as adsorbents to remove cationic dyes such as MB and MG in the aqueous solution. With merely  $5 \text{ mg}$  of adsorbent and  $5 \text{ mg L}^{-1}$  dye concentration, the removal efficiency reached approximately  $\sim 98\%$  for both dyes in just 2 min. Even for higher concentrations, the removal efficiency was around 98.8% for MB and 96.6% for MG in 6 and 10 min, respectively, with the same adsorbent dosage. The adsorption data were fitted to various kinetic and isothermal models to get insight into the adsorption mechanism and behavior. The pseudo-second-order kinetic model and the Redlich–Peterson model best fit the experimental data, showing that multi-layer adsorption and chemisorption were the primary adsorption mechanisms. The GS-CNSs also showed high surface area and high adsorption capacity for both dyes. This implies that these CNSs could be a promising alternative for wastewater treatment and dye removal mitigation. The use of groundnut skin as a precursor material for CNS synthesis also suggests a sustainable and cost-effective approach. The adsorption was a highly

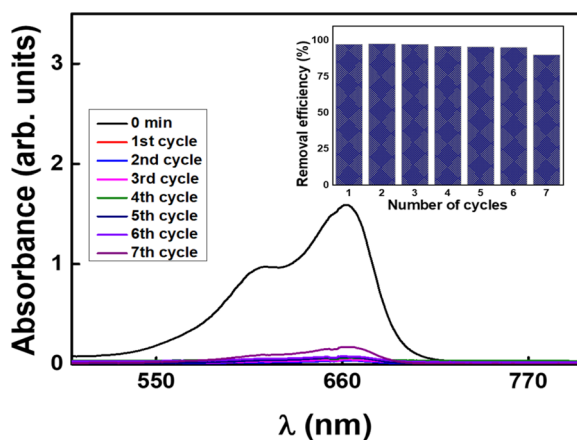


Fig. 10 Absorbance spectra of treated MB dye samples in reusability study; the inset shows GS-CNSs showing the number of adsorption cycles.

efficient and cost-effective method for the fast removal of cationic dyes. However, it is worth noting that the achieved removal efficiency of 48% using a membrane leaves room for further improvement in dye removal using a membrane system. Additional research is necessary to enhance the performance of the membrane system and achieve higher removal efficiencies. Factors such as membrane composition, surface modifications, and optimization of operating conditions should be explored to enhance the membrane's dye adsorption and removal capabilities. Further research in this direction to optimize the membrane system and understand the underlying mechanisms is in progress and will be reported elsewhere.

## Author contributions

Aman Sharma: conceptualization, investigation, methodology, data curation, formal analysis, writing—draft manuscript, writing—original draft, revision of the manuscript and editing, writing—review and editing. Jyothi Mannekote Shivanna: revision of the manuscript and editing, supervision, formal analysis, reviewing, and final approval of the manuscript to be published. Abdullah N. Alodhayb: revision of the manuscript and editing, reviewing, and final approval of the manuscript to be published. Gurumurthy Hegde: revision of the manuscript and editing, supervision, validation, formal analysis, reviewing, and final approval of the manuscript to be published.

## Conflicts of interest

There are no conflicts to declare.

## Acknowledgements

One of the authors, Gurumurthy Hegde, thanks the Centre for Research Projects, CHRIST (Deemed to be University) for providing financial support with grant number SMSS-2214. Another author Abdullah N. Alodhayb acknowledges Researchers Supporting Project number (RSP2024R304), King Saud University, Riyadh, Saudi Arabia.

## References

- 1 F. Amalina, A. S. Abd Razak, S. Krishnan, A. W. Zularisam and M. Nasrullah, *Cleaner Waste Syst.*, 2022, **3**, 100051, DOI: [10.1016/j.clwas.2022.100051](https://doi.org/10.1016/j.clwas.2022.100051).
- 2 M. M. Hassan and C. M. Carr, *Chemosphere*, 2021, **265**, 129087, DOI: [10.1016/j.chemosphere.2020.129087](https://doi.org/10.1016/j.chemosphere.2020.129087).
- 3 N. Kaya and Z. Y. Uzun, *Biomass Convers. Biorefin.*, 2020, **11**, 1067–1083, DOI: [10.1007/s13399-020-01063-8](https://doi.org/10.1007/s13399-020-01063-8).
- 4 N. P. Raval, P. U. Shah and N. K. Shah, *Appl. Water Sci.*, 2016, **7**, 3407–3445, DOI: [10.1007/s13201-016-0512-2](https://doi.org/10.1007/s13201-016-0512-2).
- 5 S. J. Culp, L. R. Blankenship, D. F. Kusewitt, D. R. Doerge, L. T. Mulligan and F. A. Beland, *Chem.–Biol. Interact.*, 1999, **122**, 153–170, DOI: [10.1016/s0009-2797\(99\)00119-2](https://doi.org/10.1016/s0009-2797(99)00119-2).
- 6 C. J. Cha, D. R. Doerge and C. E. Cerniglia, *Appl. Environ. Microbiol.*, 2001, **67**, 4358–4360, DOI: [10.1128/AEM.67.9.4358-4360.2001](https://doi.org/10.1128/AEM.67.9.4358-4360.2001).
- 7 P. Ganguly, R. Sarkhel and P. Das, *Surf. Interfaces*, 2020, **20**, 100616, DOI: [10.1016/j.surfin.2020.100616](https://doi.org/10.1016/j.surfin.2020.100616).
- 8 Y.-R. Lin, Y.-F. Hu, C.-Y. Huang, H.-T. Huang, Z.-H. Liao, A.-T. Lee, Y.-S. Wu and F.-H. Nan, *Front. Environ. Sci.*, 2022, **10**, 1–9, DOI: [10.3389/fenvs.2022.906886](https://doi.org/10.3389/fenvs.2022.906886).
- 9 A. H. Jawad, R. Razuan, J. N. Appaturi and L. D. Wilson, *Surf. Interfaces*, 2019, **16**, 76–84, DOI: [10.1016/j.surfin.2019.04.012](https://doi.org/10.1016/j.surfin.2019.04.012).
- 10 H. Chandarana, P. Senthil Kumar, M. Seenuvasan and M. Anil Kumar, *Chemosphere*, 2021, **285**, 131480, DOI: [10.1016/j.chemosphere.2021.131480](https://doi.org/10.1016/j.chemosphere.2021.131480).
- 11 A. Waheed, N. Baig, N. Ullah and W. Falath, *J. Environ. Manage.*, 2021, **287**, 112360, DOI: [10.1016/j.jenvman.2021.112360](https://doi.org/10.1016/j.jenvman.2021.112360).
- 12 L. Soldatkina and M. Yanar, *ChemEngineering*, 2023, **7**, 6, DOI: [10.3390/chemengineering7010006](https://doi.org/10.3390/chemengineering7010006).
- 13 M. M. Aljumaily, N. S. Ali, A. E. Mahdi, H. M. Alayan, M. AlOmar, M. M. Hameed, B. Ismael, Q. F. Alsally, M. A. Alsaadi, H. S. Majdi and Z. B. Mohammed, *Water*, 2022, **14**, 1396, DOI: [10.3390/w14091396](https://doi.org/10.3390/w14091396).
- 14 A. T. Mansour, A. E. Alprol, K. M. Abualnaja, H. S. El-Beltagi, K. M. A. Ramadan and M. Ashour, *Polymers*, 2022, **14**, 1735, DOI: [10.3390/polym14071375](https://doi.org/10.3390/polym14071375).
- 15 A. K. Badawi, M. Abd Elkodous and G. A. M. Ali, *RSC Adv.*, 2021, **11**, 36528–36553, DOI: [10.1039/D1RA06892J](https://doi.org/10.1039/D1RA06892J).
- 16 N. U. M. Nizam, M. M. Hanafiah, E. Mahmoudi, A. A. Halim and A. W. Mohammad, *Sci. Rep.*, 2021, **11**, 1–17, DOI: [10.1038/s41598-021-88084-z](https://doi.org/10.1038/s41598-021-88084-z).
- 17 I. Akkari, Z. Graba, N. Bezzi, M. M. Kaci, F. A. Merzeg, N. Bait, A. Ferhati, G. L. Dotto and Y. Benguerba, *Environ. Sci. Pollut. Res. Int.*, 2023, **30**, 3027–3044, DOI: [10.1007/s11356-022-22402-4](https://doi.org/10.1007/s11356-022-22402-4).
- 18 D. Pathania, A. Araballi, F. Fernandes, J. M. Shivanna, G. Sriram, M. Kurkuri, G. Hegde and T. M. Aminabhavi, *Environ. Res.*, 2023, **224**, 115521, DOI: [10.1016/j.envres.2023.115521](https://doi.org/10.1016/j.envres.2023.115521).
- 19 A. H. Jawad, A. S. Abdulhameed and M. S. Mastuli, *J. Taibah Univ. Sci.*, 2020, **14**, 305–313, DOI: [10.1080/16583655.2020.1736767](https://doi.org/10.1080/16583655.2020.1736767).
- 20 D. Pathania, V. S. Bhat, J. Mannekote Shivanna, G. Sriram, M. Kurkuri and G. Hegde, *Spectrochim. Acta, Part A*, 2022, **276**, 121197, DOI: [10.1016/j.saa.2022.121197](https://doi.org/10.1016/j.saa.2022.121197).
- 21 B. Krishnappa, V. S. Bhat, V. Ancy, J. C. Joshi, S. Jyothi M, M. Naik and G. Hegde, *Molecules*, 2022, **27**, 7017, DOI: [10.3390/molecules27207017](https://doi.org/10.3390/molecules27207017).
- 22 B. Krishnappa, S. Saravu, J. M. Shivanna, M. Naik and G. Hegde, *Environ. Sci. Pollut. Res.*, 2022, **29**, 79067–79081, DOI: [10.1007/s11356-022-21251-5](https://doi.org/10.1007/s11356-022-21251-5).
- 23 B. H. Hameed and M. I. El-Khaiary, *J. Hazard. Mater.*, 2008, **155**, 601–609, DOI: [10.1016/j.jhazmat.2007.11.102](https://doi.org/10.1016/j.jhazmat.2007.11.102).
- 24 M. A. El-Nemr, N. M. Abdelmonem, I. M. A. Ismail, S. Ragab and A. El-Nemr, *Desalin. Water Treat.*, 2020, **203**, 403–431, DOI: [10.5004/dwt.2020.26207](https://doi.org/10.5004/dwt.2020.26207).
- 25 M. A. El-Nemr, N. M. Abdelmonem, I. M. A. Ismail, S. Ragab and A. El Nemr, *Desalin. Water Treat.*, 2020, **203**, 327–355, DOI: [10.5004/dwt.2020.26190](https://doi.org/10.5004/dwt.2020.26190).

- 26 E. F. D. Januário, T. B. Vidovix, L. A. de Araújo, L. Bergamasco Beltran, R. Bergamasco and A. M. S. Vieira, *Environ. Technol.*, 2022, **43**, 4315–4329, DOI: [10.1080/09593330.2021.1946601](https://doi.org/10.1080/09593330.2021.1946601).
- 27 K. Sathya, H. Jayalakshmi, S. N. Reddy, M. V. Ratnam and D. Bandhu, *Biomass Convers. Biorefine.*, 2023, **13**(18), 1–13, DOI: [10.1007/s13399-023-05213-6](https://doi.org/10.1007/s13399-023-05213-6).
- 28 A. Vakili, A. A. Zinatizadeh, Z. Rahimi, S. Zinadini, P. Mohammadi, S. Azizi, A. Karami and M. Abdulgader, *J. Cleaner Prod.*, 2023, **382**, 134899, DOI: [10.1016/j.jclepro.2022.134899](https://doi.org/10.1016/j.jclepro.2022.134899).
- 29 S. Sunkar, P. Prakash, B. Dhandapani, O. Baigenzhenov, J. A. Kumar, V. Nachiyaar, S. Zolfaghari, S. Tejaswini and A. Hosseini-Bandegharai, *Environ. Res.*, 2023, **233**, 116486, DOI: [10.1016/j.envres.2023.116486](https://doi.org/10.1016/j.envres.2023.116486).
- 30 M. S. Jyothi, V. J. Angadi, T. V. Kanakalakshmi, M. Padaki, B. R. Geetha and K. Soontarapa, *J. Polym. Environ.*, 2019, **27**, 2408–2418, DOI: [10.1007/s10924-019-01531-x](https://doi.org/10.1007/s10924-019-01531-x).
- 31 P. Wang, Q. Ma, D. Hu and L. Wang, *Desalin. Water Treat.*, 2016, **57**, 10261–10269, DOI: [10.1080/19443994.2015.1033651](https://doi.org/10.1080/19443994.2015.1033651).
- 32 N. R. Putra, D. N. Rizkiyah, M. A. Che Yunus, A. H. Abdul Aziz, A. S. H. Md Yasir, I. Irianto, J. Jumakir, W. Waluyo, S. Suparwoto and L. Qomariyah, *Molecules*, 2023, **28**, 4325, DOI: [10.3390/molecules28114325](https://doi.org/10.3390/molecules28114325).
- 33 C. Lavanya, K. Soontarapa, M. S. Jyothi and R. Geetha Balakrishna, *Sep. Purif. Technol.*, 2019, **211**, 348–358, DOI: [10.1016/j.seppur.2018.10.006](https://doi.org/10.1016/j.seppur.2018.10.006).
- 34 J. Deng, M. Li and Y. Wang, *Green Chem.*, 2016, **18**, 4824–4854, DOI: [10.1039/C6GC01172A](https://doi.org/10.1039/C6GC01172A).
- 35 A. Nieto-Márquez, R. Romero, A. Romero and J. L. Valverde, *J. Mater. Chem.*, 2011, **21**, 1664–1672, DOI: [10.1039/C0JM01350A](https://doi.org/10.1039/C0JM01350A).
- 36 S. Yallappa, D. R. Deepthi, S. Yashaswini, R. Hamsanandini, M. Chandraprasad, S. Ashok Kumar and G. Hegde, *Nano-Struct. Nano-Objects*, 2017, **12**, 84–90, DOI: [10.1016/j.nanoso.2017.09.009](https://doi.org/10.1016/j.nanoso.2017.09.009).
- 37 S. Supriya, A. Divyashree, S. Yallappa and G. Hegde, *Mater. Today*, 2018, **5**, 2907–2911, DOI: [10.1016/j.matpr.2018.01.085](https://doi.org/10.1016/j.matpr.2018.01.085).
- 38 G. Hegde, S. A. Abdul Manaf, A. Kumar, G. A. M. Ali, K. F. Chong, Z. Ngaini and K. V. Sharma, *ACS Sustainable Chem. Eng.*, 2015, **3**, 2247–2253, DOI: [10.1021/acssuschemeng.5b00517](https://doi.org/10.1021/acssuschemeng.5b00517).
- 39 M. Zhang, L. Chang, Y. Zhao and Z. Yu, *Arabian J. Sci. Eng.*, 2019, **44**, 111–121, DOI: [10.1007/s13369-018-3258-3](https://doi.org/10.1007/s13369-018-3258-3).
- 40 J. Pal and M. K. Deb, *Appl. Nanosci.*, 2013, **4**, 967–978, DOI: [10.1007/s13204-013-0277-y](https://doi.org/10.1007/s13204-013-0277-y).
- 41 A. T. Ojedokun and O. S. Bello, *Appl. Water Sci.*, 2016, **7**, 1965–1977, DOI: [10.1007/s13201-015-0375-y](https://doi.org/10.1007/s13201-015-0375-y).
- 42 I. J. Idan, S. N. A. B. Jamil, L. C. Abdullah and T. S. Y. Choong, *Int. J. Chem. Eng.*, 2017, 1–13, DOI: [10.1155/2017/9792657](https://doi.org/10.1155/2017/9792657).
- 43 A. H. Jawad, A. S. Abdulhameed, L. D. Wilson, S. S. Syed-Hassan, Z. A. ALOthman and M. R. Khan, *Chin. J. Chem. Eng.*, 2021, **32**, 281–290, DOI: [10.1016/j.cjche.2020.09.070](https://doi.org/10.1016/j.cjche.2020.09.070).
- 44 K. A. Tan, N. Morad and J. Q. Ooi, *Int. J. Environ. Sci. Dev.*, 2016, **7**, 724–728, DOI: [10.18178/IJESD.2016.7.10.869](https://doi.org/10.18178/IJESD.2016.7.10.869).
- 45 R. S. Almufarij, B. Y. Abdulkhair, M. Salih, H. Aldosari and N. W. Aldayel, *Molecules*, 2022, **27**, 4577, DOI: [10.3390/molecules27144577](https://doi.org/10.3390/molecules27144577).
- 46 A. S. Dehghan, M. Hassannezhad, M. Hosseini and M. R. Ganjali, *J. Serb. Chem. Soc.*, 2019, **84**, 701–712, DOI: [10.2298/JSC181228038D](https://doi.org/10.2298/JSC181228038D).
- 47 Y.-C. Lee, J.-Y. Kim and H.-J. Shin, *Sep. Sci. Technol.*, 2013, **48**, 1093–1101, DOI: [10.1080/01496395.2012.723100](https://doi.org/10.1080/01496395.2012.723100).
- 48 J. Wang and X. Guo, *J. Hazard. Mater.*, 2020, **390**, 122156, DOI: [10.1016/j.jhazmat.2020.122156](https://doi.org/10.1016/j.jhazmat.2020.122156).
- 49 M. Benjelloun, Y. Miyah, G. A. Evrendilek, F. Zerrouq and S. Lairini, *Arabian J. Chem.*, 2021, **14**, 103031, DOI: [10.1016/j.arabjc.2021.103031](https://doi.org/10.1016/j.arabjc.2021.103031).
- 50 I. Langmuir, *J. Am. Chem. Soc.*, 1918, **40**, 1361–1403, DOI: [10.1021/ja02242a004](https://doi.org/10.1021/ja02242a004).
- 51 N. Ayawei, A. N. Ebelegi and D. Wankasi, *J. Chem.*, 2017, **11**, 1–11, DOI: [10.1155/2017/3039817](https://doi.org/10.1155/2017/3039817).
- 52 N. Ayawei, S. S. Angaye, D. Wankasi and E. D. Dikio, *Open Phys. Chem. J.*, 2015, **5**, 56–70, DOI: [10.4236/ojpc.2015.53007](https://doi.org/10.4236/ojpc.2015.53007).
- 53 H. Shahbeig, N. Bagheri, S. Ghorbanian, A. Hallajisani and S. Pourkarimi, *World J. Model. Simul.*, 2013, **9**, 243–254.
- 54 B. R. Vergis, N. Kottam, R. Hari Krishna and B. M. Nagabhushana, *Nano-Struct. Nano-Objects*, 2019, **18**, 100290, DOI: [10.1016/j.nanoso.2019.100290](https://doi.org/10.1016/j.nanoso.2019.100290).
- 55 F. Brouers and T. J. Al-Musawi, *J. Mol. Liq.*, 2015, **212**, 46–51, DOI: [10.1016/j.molliq.2015.08.054](https://doi.org/10.1016/j.molliq.2015.08.054).
- 56 F. Gimbert, N. Morin-Crini, F. Renault, P.-M. Badot and G. Crini, *J. Hazard. Mater.*, 2008, **157**, 34–46, DOI: [10.1016/j.jhazmat.2007.12.072](https://doi.org/10.1016/j.jhazmat.2007.12.072).
- 57 J. Wang and X. Guo, *Chemosphere*, 2020, **258**, 127279, DOI: [10.1016/j.chemosphere.2020.127279](https://doi.org/10.1016/j.chemosphere.2020.127279).
- 58 H. Moussout, H. Ahlafi, M. Aazza and H. Maghat, *Karbala Int. J. Mod. Sci.*, 2018, **4**, 244–254, DOI: [10.1016/j.kijoms.2018.04.001](https://doi.org/10.1016/j.kijoms.2018.04.001).
- 59 L. Meng, X. Zhang, Y. Tang, K. Su and J. Kong, *Sci. Rep.*, 2015, **5**, 7910, DOI: [10.1038/srep07910](https://doi.org/10.1038/srep07910).
- 60 J. Jaafari, H. Barzanouni, S. Mazloomi, N. Amir Abadi Farahani, K. Sharafi, P. Soleimani and G. A. Haghighat, *Int. J. Biol. Macromol.*, 2020, **164**, 344–355, DOI: [10.1016/j.ijbiomac.2020.07.042](https://doi.org/10.1016/j.ijbiomac.2020.07.042).